Electronic Structure and Optical Properties of Cu_{2}ZnGeSe_{4}: First-Principles Calculations and Vacuum-Ultraviolet Spectroscopic Ellipsometric Studies

S. G. Choi, J.-S. Park, A. L. Donohue, S. T. Christensen, B. To, C. Beall, S.-H. Wei, and I. L. Repins

Phys. Rev. Applied **4**, 054006 — Published 19 November 2015

DOI: 10.1103/PhysRevApplied.4.054006

Electronic structure and optical properties of $Cu_2ZnGeSe_4$: First-principles calculations and vacuum-ultraviolet spectroscopic ellipsometric studies

S.G. Choi,[1,a)] J.-S. Park,[1] A.L. Donohue,[2] S.T. Christensen,[1] B. To,[1] C. Beall,[1] S.-H. Wei,[1] and I.L. Repins[1]

[1]*National Renewable Energy Laboratory, Golden, Colorado 80401, USA*
[2]*J.A. Woollam Co. Inc., Lincoln, Nebraska 68508, USA*

ABSTRACT

$Cu_2ZnGeSe_4$ is of interest for the development of next-generation thin-film photovoltaic technologies. To understand its electronic structure and related fundamental optical properties, we performed *first-principles* calculations for three structural variations: kesterite, stannite, and primitive-mixed CuAu phases. The calculated data are compared with the room-temperature dielectric function $\varepsilon = \varepsilon_1 + i\varepsilon_2$ spectrum of polycrystalline $Cu_2ZnGeSe_4$ determined by vacuum-ultraviolet spectroscopic ellipsometry in the photon-energy range of 0.7 to 9.0 eV. Ellipsometric data are modeled with the sum of eight Tauc-Lorentz oscillators, and the best-fit model yields the bandgap and Tauc-gap energies of 1.25 and 1.19 eV, respectively. A comparison of overall peak shapes and relative intensities between experimental spectra and the calculated ε data for three structural variations suggests that the sample may not have a pure (ordered) kesterite phase. The complex refractive index $N = n + ik$, normal-incidence reflectivity R, and absorption coefficients α are calculated from the modeled ε spectrum, which are also compared with those of $Cu_2ZnSnSe_4$. The spectral features for $Cu_2ZnGeSe_4$ appear to be weaker and broader than those for $Cu_2ZnSnSe_4$, which is possibly due to more structural imperfections presented in $Cu_2ZnGeSe_4$ than $Cu_2ZnSnSe_4$.

[a)] Author to whom correspondence should be addressed. Electronic mail: feelingmn@gmail.com.

I. INTRODUCTION

$Cu_2ZnSnSe_4$ has been of interest for its application in next-generation thin-film photovoltaic technology [1]. Although the power conversion efficiency (PCE) of $Cu_2ZnSnSe_4$ devices has increased rapidly over the past few years, the record PCE (11.6%) [2] is still much lower than those of CdTe (21.0 %) and $Cu(In,Ga)Se_2$ (21.7 %) solar cells [3]. The optimum bandgap energy E_0 of an absorber material for high-performance solar cells is known to be in the range of 1.1 to 1.4 eV [4]. Thus, it has been attempted to increase the E_0 of $Cu_2ZnSnSe_4$ (0.97 eV) [5] by alloying it with S and forming the $Cu_2ZnSnS_xSe_{4-x}$ quinary compound, which indeed made a noticeable improvement of the PCE to 12.6% [6].

$Cu_2ZnGeSe_4$ formed by replacing Sn in $Cu_2ZnSnSe_4$ with Ge can be considered another way to increase the E_0. Use of Ge rather than S, to expand the E_0, also possesses a few additional advantages. First, the (Ge,Sn) alloy has lower formation energy than the (S,Se) alloy, so it can be formed more easily [7,8]. Second, the E_0 expansion with Ge alloying is caused mostly by the upward shift of the conduction-band minimum (CBM) [7], whereas 30% expansion of the E_0 achieved with S alloying is due to the downward shift of the valence-band maximum (VBM) [8]. Consequently, the alternate alloying approaches enable a comparison of devices with a similar E_0 but different conduction band offsets to the buffer, which will help us better understand the carrier recombination mechanisms at the buffer/absorber interface. Third, use of Ge allows the E_0 expansion without preferential segregation of the alloying elements to a secondary phase. There is widespread agreement in the literature that excess Zn (Zn/Sn ~ 1.2) is needed to make high-performance $Cu_2ZnSn(S,Se)_4$-based solar cells [9]. However, the excess Zn results in a measurable amount of Zn(S,Se) precipitates even in the highest-quality absorbers [10,11,12,13,14]. The formation of ZnS is thermodynamically more favorable than that of ZnSe because its formation energy is substantially more negative. Therefore, it is likely that the Zn-binary compound preferentially displaces S from the crystal lattice sites in a $Cu_2ZnSn(S,Se)_4$ absorber, which possibly leads to the observed harmful local fluctuations of E_0 [15]. Ge-induced enhancement in device performance has indeed been demonstrated from nanocrystal-based $Cu_2Zn(Sn,Ge)(S,Se)_4$ devices with a PCE of 9.4% [16] and hydrazine-based $Cu_2Zn(Sn,Ge)Se_4$ devices with a PCE of 9.1% [17].

To optimize solar cell structure and improve the device performance through *bandgap engineering*, it is important to understand a material's electronic structure and related fundamental optical properties such as complex dielectric function $\varepsilon = \varepsilon_1 + i\varepsilon_2$ and complex refractive index $N = n + ik$ [18,19]. Accurate optical information can be obtained from a systematic comparison study of the electronic structure calculations and spectroscopic measurements [20,21].

Here, we present the electronic energy band structure and complex dielectric function $\varepsilon = \varepsilon_1 + i\varepsilon_2$ spectra of $Cu_2ZnGeSe_4$ obtained from *first-principles* calculations for three structural variations: kesterite (KS), stannite (ST), and primitive-mixed CuAu phases (PMCA). The calculated data are compared with the ε spectrum of a polycrystalline $Cu_2ZnGeSe_4$ thin film determined by spectroscopic ellipsometry (SE) over the photon-energy range of 0.7 to 9.0 eV. SE is known to be a highly suitable method of determining ε and N spectra of semiconductors [22], and therefore, it has been used to characterize the optical properties of many solar cell absorber materials including CdTe [23,24], $CuInGaSe_2$ [25,26,27], Cu_2ZnSnS_4 [28,29], and $Cu_2ZnSnSe_4$ [5,30,31,32]. For $Cu_2ZnGeSe_4$, León *et al*. [33] reported room-temperature optical function spectra of bulk crystals. Due to the limited spectral range (1.2–4.6 eV), however, no bandgap onset was resolved and only three optical structures were analyzed using Adachi's Model Dielectric Function (MDF) method [34]. Our SE data exhibit multiple optical structures associated with the electronic interband transitions and the optical gap where the ε_2 and *k* vanish. Complex refractive index N = n + ik, normal-incidence reflectivity R, and absorption coefficients α are also calculated from the modeled ε spectrum, which are compared with the published data for $Cu_2ZnSnSe_4$ [5].

II. DENSITY-FUNCTIONAL THEORY CALCULATIONS

It has long been considered that $Cu_2ZnSnSe_4$ crystals form with the KS phase and are still called simply "kesterite solar cells" mainly because electronic structure calculations show that the KS is thermodynamically the most stable phase for $Cu_2ZnSnSe_4$ [35,36]. However, the formation energy for ST and PMCA phases are higher than that for the KS phase by only a few meV/atom [35,36]. Thus, in practice, $Cu_2ZnSnSe_4$ thin films can form with a mix of the three structural phases (KS, ST, and PMCA) or their disordered version, depending on the growth methods and conditions [37]. In fact, there are several experimental evidences [38,39,40] showing that the crystal structure of typical $Cu_2ZnSnSe_4$ thin films is not the pure (ordered) KS phase.

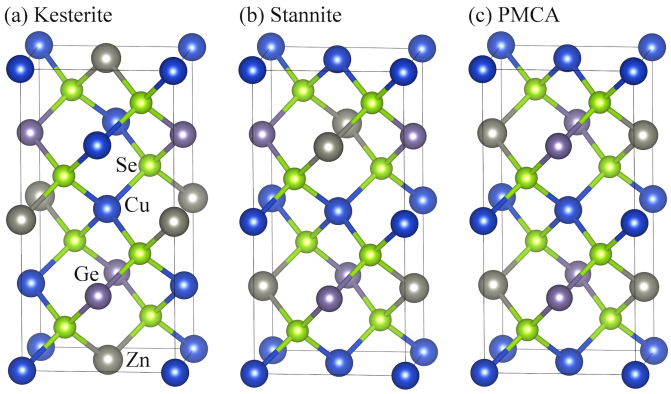

Figure 1. Atomic structure of kesterite (KS), stannite (ST), and primitive-mixed CuAu (PMCA) phases. Blue, purple, gray, and green colors represent Cu, Zn, Ge, and Se atoms, respectively. The KS and ST phases have the body-centered tetragonal unit cell, whereas the PMCA phase has the tetragonal unit cell.

Owing to its structural and chemical similarities with $Cu_2ZnSnSe_4$, $Cu_2ZnGeSe_4$ is also expected to grow in one of the three possible structures, KS, ST, and PMCA, shown in Figs. 1(a) through 1(c), or their disordered form. As for $Cu_2ZnSnSe_4$, it is also predicted that KS is thermodynamically the most stable phase and the PMCA is the least stable phase for $Cu_2ZnGeSe_4$. We found that the formation energies for the ST and PMCA phases are higher than that for the KS phase by 7 and 19 meV/atom, respectively. Our results are slightly higher than the values reported in previous study (5 and 11 meV/atom) [41], but the trend is the same.

The electronic structure and ε spectrum for each phase of $Cu_2ZnGeSe_4$ were obtained by *first-principles* density-functional theory (DFT) calculations using the hybrid functional proposed by Heyd, Scuseria, and Ernzerhof (HSE) [42] as implemented in the VASP code [43]. The screening parameter of $\omega = 0.2$ Å^{-1} and the exchange parameter of $\alpha = 0.25$ are used. The cutoff energy for the plane-wave basis is 295 eV. The lattice parameters and the internal coordinates are fully relaxed until the residual force becomes smaller than 0.05 eV/Å. For the relaxation of the atomic structure, an 8×8×8 k-point grid is used for Brillouin zone (BZ) integration. To calculate the ε_2 data, a denser k-point grid was used: 10×10×10 for KS and ST phases, and 12×12×12 for the PMCA phase. The ε_1 was then calculated by the Kramers-Krönig (K-K) transformation of the ε_2 with a small complex shift of 0.1 eV to make the spectrum smooth for the given k-point meshes.

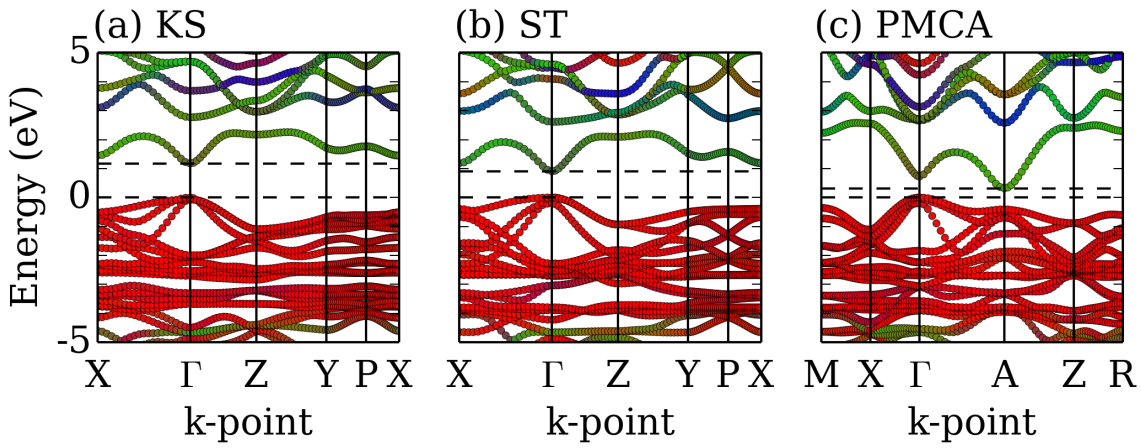

Figure 2. The electronic band structures of (a) KS-, (b) ST-, and (c) PMCA-phase $Cu_2ZnGeSe_4$. The dashed horizontal lines correspond to the band edge positions (i.e., conduction-band minimum and valence-band maximum). Red, green, and blue colors represent the contributions from Cu, Ge, and Zn characters, respectively, among the cations. Valence band maximum is set to 0 eV.

The calculated electronic energy band structures of $Cu_2ZnGeSe_4$ with KS-, ST-, and PMCA-phase are presented in Figs. 2(a) through 2(c). For KS and ST phases, the bandgap is direct as VBM and CBM collocate at the Γ point of BZ. The calculated E_0 values for KS and ST phases are 1.180 and 0.954 eV, respectively. However, the PMCA phase has an indirect

bandgap because the CBM is at the A point whereas the VBM is at the Γ point. The difference between the calculated direct (0.761 eV) and indirect (0.356 eV) bandgaps is 0.405 eV. The direct-indirect bandgap transition in $Cu_2ZnGeSe_4$ has also been predicted in a previous theoretical study [7]. The details of the ordering-induced direct-indirect bandgap transitions are discussed elsewhere [44]. The lattice parameters used in our calculations and the resulting E_0 for three structural phases are summarized in Table I. Our calculated lattice parameters are approximately 1% larger than the reported values [45].

TABLE I. The in-plane (*a*) and out-of-plane (*c*) lattice parameters used in the density-functional theory calculations, and the calculated bandgap energies (E_0) of $Cu_2ZnGeSe_4$ for three structural phases. The KS and ST phases possess direct bandgaps whereas the PMCA phase has an indirect bandgap.

Structural phase	*a* (Å)	*c* (Å)	E_0 (eV)
KS	5.621	11.145	1.180 (direct)
ST	5.580	11.286	0.954 (direct)
PMCA	5.573	5.643	0.356 (indirect) 0.761 (direct)

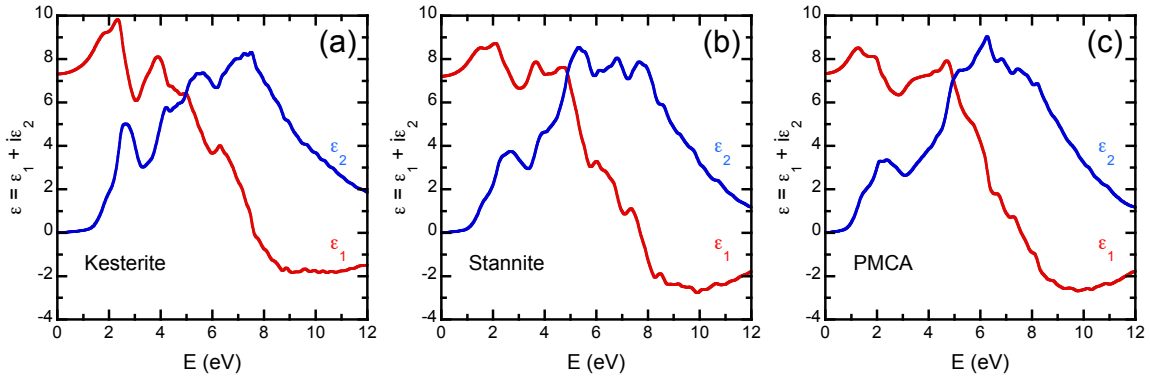

Figure 3. The calculated $\varepsilon = \varepsilon_1 + i\varepsilon_2$ data for (a) kesterite (KS), (b) stannite (ST), and (c) primitive-mixed CuAu (PMCA) phases of $Cu_2ZnGeSe_4$. Real (ε_1) and imaginary (ε_2) parts are shown as solid red and blue lines, respectively.

Figures 3(a) through 3(c) show the calculated ε spectra for KS-, ST-, and PMCA-phase $Cu_2ZnGeSe_4$. These spectra are a mathematical average of the ε components along the three principal axes, $(2\varepsilon_a + \varepsilon_c)/3$, so that the optical function spectra of the polycrystalline material are properly described. Overall, the ε_2 spectra for three structural phases shown in solid blue lines are similar and they all consist of a relatively weak but distinct structure at around 2.5 eV and a main broad structure spanning from 5 to 12 eV. However, one major difference in the ε_2 spectra between the KS phase and the other

two phases is the relative intensity of optical structure at ~2.5 eV with respect to the main broad structure. Although it appears as a *bump-like* feature for the ST and PMCA phases, this structure is more prominent for the KS phase.

The observed variation in transition strength of the structure at ~2.5 eV can be understood by the differences in electronic energy band structure among the three structural phases. As expressed in Eq. (1), the joint density of electronic states D_j increases as the denominator $|\nabla_k(E_c - E_v)|$ decreases. The term $|\nabla_k(E_c - E_v)|$ vanishes mathematically when the conduction and valence bands have the same tangent at the same k-point. Those highly symmetric points in the BZ are called the *Van Hove singularities* or *critical points* [46].

$$D_j(E_{cv}) = \frac{1}{4\pi^3}\int \frac{dS_k}{\left|\nabla_k(E_c - E_v)\right|} \qquad (1)$$

In Figs. 4(a) through 4(c), the energy differences between the various E_c and E_v bands ($E_c - E_v$) are plotted. The dashed horizontal line in each figure indicates the energy difference of 2.5 eV. The KS phase shown in Fig. 4(a) has several *flat* segments near the horizontal line between the Y and P points of BZ, which suggests multiple transitions occurring at around 2.5 eV. This is probably the origin of the relatively strong optical structure at ~2.5 eV observed in the ε_2 spectrum for the KS phase. For the other two phases (Figs. 4(b) and 4(c)), not many transitions are seen near the horizontal line other than just a few at the Γ point.

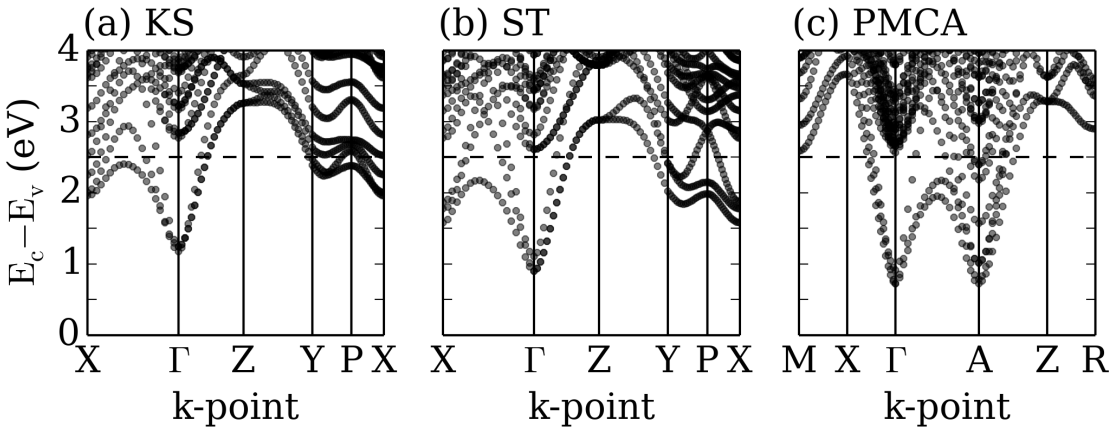

Figure 4. The energy difference between conduction and valence bands, $\Delta E = E_c - E_v$ for (a) KS-, (b) ST-, and (c) PMCA-phase $Cu_2ZnGeSe_4$. The dashed horizontal lines indicate the ΔE of 2.5 eV.

III. EXPERIMENTS

A polycrystalline $Cu_2ZnGeSe_4$ thin film was grown by thermal co-evaporation of elemental Cu, Zn, Ge, and Se. The deposition uses the same equipment and method as that detailed for device-quality $Cu_2ZnSnSe_4$ growth [47], with two modifications: 1) GeSe source material replaces Sn in one thermal evaporation boat, and 2) the substrate temperature is limited to 385°C due to the high vapor pressure of GeSe compared to SnSe. It is well known that $Cu_2ZnGeSe_4$, $Cu_2ZnSnSe_4$, Cu_2ZnSnS_4 and related alloys require overpressure of chalcogen and the group-IV chalcogenide, such as SnSe and GeSe, to be stabilized with applied heat under vacuum [48,49]. The high rejection rate of GeSe from the sample and the maximum rate at which our evaporation sources can supply GeSe thus limit the substrate temperature to 385°C. The sample used in this study was grown to a 4.3 μm on the roughened surface of soda-lime glass. Chemical composition was determined by X-ray fluorescence that was pre-calibrated by inductively coupled plasma optical emission spectrometry. The film measured 22.6 atomic % Cu, 15.1% Zn, 11.8% Ge, and 50.2% Se, which is typical of the slightly Cu-poor Zn-rich films used for kesterite solar cells [50].

Solar cells were fabricated using similar films (thinner but same process) on standard molybdenum-coated soda-lime glass substrates. The finished devices exhibited an open-circuit voltage V_{oc} of ~420 mV, a substantial fraction of the bandgap, which is another positive indication of the film quality. A typical diode current-voltage curve from one of these $Cu_2ZnGeSe_4$ devices is shown in the supplemental materials document [51].

Structural properties of the film were characterized by X-ray diffraction (XRD) and Raman scattering (RS) spectroscopy. The XRD measurements were done using a Rigaku DMAX instrument with a rotating Cu anode operated at 40 kV and 250 mA. Slit collimation and a graphite post-monochromator were used to select diffracted Cu-Kα radiation. Calculated data were obtained by using the CrystalMaker® 8.7.5/CrystalDiffract® 6.0.0 software platform. Raman scattering (RS) spectra were taken at room temperature using a Renishaw inVia reflex microscope system equipped with a Peltier-cooled charge-coupled device array. The excitation wavelength was 532 nm and the power was lower than 2.5 mW.

A thin film grown on a roughened surface becomes a bulk crystal optically because the rough surface suppresses the reflection of probing light from the film/substrate interface. The main benefit here is that no thickness fringe appears in the raw SE data, and the optical information around the bandgap can be assessed directly without a mathematical correction of data in the ideal case. Details of this *pseudobulk* method are given in Ref. 5. Prior to SE measurements, the surface of the $Cu_2ZnGeSe_4$ film was chemo-mechanically polished using a colloidal silica suspension with 0.02-μm particles in an attempt to reduce the microscopic roughness of the surface [5,38]. A cross-sectional scanning electron

micrograph of the polished $Cu_2ZnGeSe_4$ film grown on the roughened glass substrate is provided in the supplemental materials document [51].

Vacuum ultraviolet (VUV) SE data were collected in the photon-energy range of 0.7 to 9.0 eV with the sample maintained at room temperature by using a spectroscopic rotating analyzer-type ellipsometer equipped with a computer-controlled MgF_2 Berek compensator (VUV-VASE model, J.A. Woollam, Co., Inc.). The system was continuously purged with dry nitrogen gas to avoid the absorption of light above 6.5 eV by oxygen and water vapor in the ambient. Each data point was recorded after a minimum of 300 analyzer revolutions to improve the signal-to-noise ratio. The spectral resolution is 0.01 eV and the angle of incidence was 70°.

IV. EXPERIMENTAL RESULTS AND DISCUSSION

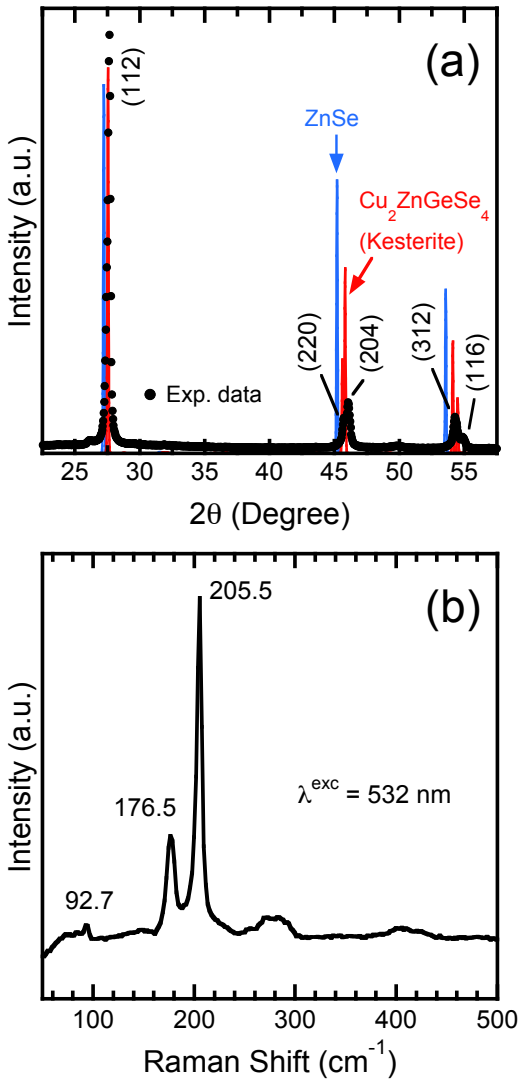

Figure 5. (a) X-ray diffraction data collected on the polished $Cu_2ZnGeSe_4$ film. Black solid circles are experimental data. Blue and red solid lines represent the calculated profiles for the ZnSe and $Cu_2ZnGeSe_4$ (kesterite phase), respectively. (b) Non-polarized Raman scattering spectrum of $Cu_2ZnGeSe_4$ taken at room temperature using an excitation wavelength of 532 nm.

The measured XRD curve is presented in Fig. 5(a) as black solid circles. The 2θ angles for the observed diffraction peaks were used to extract the lattice parameters of a = 5.608(7) Å and c = 11.077(2) Å, which are slightly smaller than the calculated values listed in Table I but are in good agreement with previously reported data [45,52,53]. Our experimental curve matches well with the calculated diffraction curve, shown as a red solid line, for $Cu_2ZnGeSe_4$. The diffraction peaks for all three phases, KS, ST, and PMCA, appear at very similar angular positions. Only the KS-phase diffraction curve is included in Fig. 5(a) for clarity. Unlike the case of $Cu_2ZnSnSe_4$, the diffraction peaks for $Cu_2ZnGeSe_4$ are clearly separated from those for ZnSe (blue solid line). No ZnSe diffraction peak is seen in our experimental XRD data.

The non-polarized room-temperature RS spectrum of $Cu_2ZnGeSe_4$ taken at the excitation wavelength of 532 nm is shown in Fig. 5(b). The observation of two dominant peaks at 176.5 and 205.5 cm^{-1} is consistent with the results from previous RS studies [54,55] of $Cu_2ZnGeSe_4$. The two peaks have been identified as the A symmetry modes from a polarization-dependent RS study [54]. A weak signal at 92.7 cm^{-1} is attributed to the E^2 (TO + LO) symmetry mode, and multiple contributions observed between 250 and 300 cm^{-1} are attributed to the E and B symmetry modes [54]. No secondary phases were detected by XRD and RS. However, since the Raman cross-section of ZnSe for non-resonant Raman is small, the presence of ZnSe secondary phase cannot be completely excluded from the RS data.

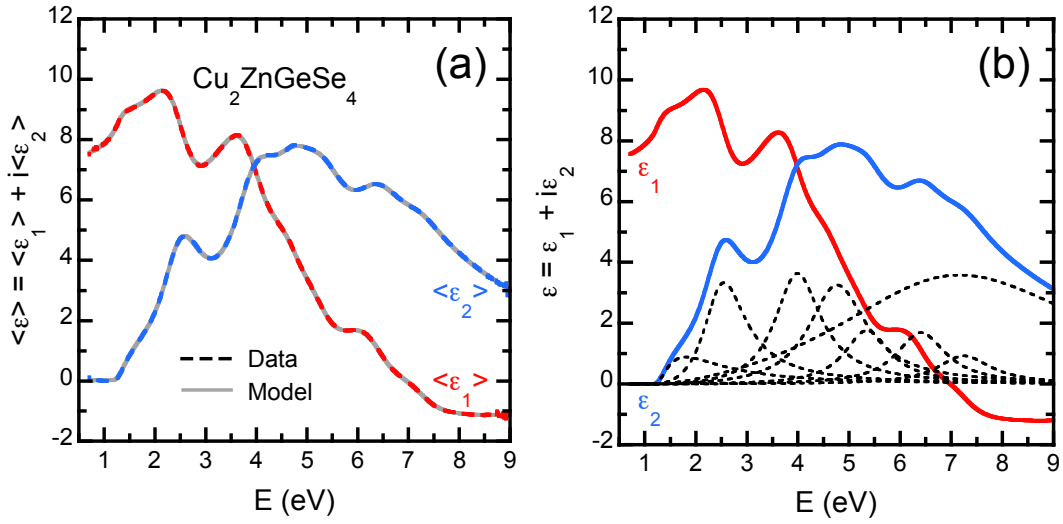

Figure 6. (a) Data (dashed color lines) and the best-fit curves (solid gray lines) for <ε> of $Cu_2ZnGeSe_4$. The best-fit curves were obtained by analyzing the data with the three-phase model (ambient/surface roughness/$Cu_2ZnGeSe_4$). (b) The modeled ε spectrum of $Cu_2ZnGeSe_4$ with the eight constituent Tauc-Lorentz oscillators.

Results from SE measurements are displayed in Fig. 6. The SE data were analyzed with the three-phase model consisting of the ambient, a surface overlayer, and the $Cu_2ZnGeSe_4$ crystal, which is essentially the same as modeling SE data of bulk crystals. The optical function data of soda-lime glass (substrate) and the thickness of $Cu_2ZnGeSe_4$ film are not required in our model because the reflections from the film/substrate interface are effectively suppressed by the use of the pseudobulk method [5], as mentioned in Sec. III.

A surface overlayer is presumably composed of microscopic roughness and native oxides, whose optical response can be represented by the Bruggeman effective medium approximation (BEMA) [56] using a 50-50 mix of the underlying material and void. The best result with minimum discrepancy between the experimental data and the model was obtained with a 3.1-Å-thick BEMA layer. As pointed out by Nelson *et al*. [57], the contributions from microscopic roughness and native oxides to a very thin BEMA layer are indistinguishable in practice.

The ε spectrum of $Cu_2ZnGeSe_4$ was constructed by the sum of eight Tauc-Lorentz (T-L) oscillators and the fit-determined $\varepsilon_1(\infty)$. The ε_2 of an individual T-L oscillator is expressed by [58]:

$$\varepsilon_2 = \begin{cases} \dfrac{AE_0C(E-E_g)^2}{(E^2-E_0^2)^2+C^2E^2}\cdot\dfrac{1}{E} & (E > E_g) \\ 0 & (E \le E_g) \end{cases} \quad (2)$$

where A is the oscillator strength, C is a broadening parameter, E_0 is the resonance energy, and E_g is the Tauc gap (the onset of absorption). The E_g was obtained from the best-fit parameters for oscillator No. 1 and set to be the same for all the other T-L oscillators. The E_g was constrained to be smaller than the E_0 by definition. The mathematical expression for the corresponding ε_1 can be calculated by the K-K integration of ε_2. As seen in Fig. 6(a), the experimental data (pseudodielectric function $\langle\varepsilon\rangle = \langle\varepsilon_1\rangle + i\langle\varepsilon_2\rangle$) and the best-fit curves are in excellent agreement. The modeled ε spectrum is presented in Fig. 6(b) with the constituent T-L oscillators. Several above-bandgap optical structures observed in the ε spectrum are associated with the electronic interband transitions [46]. We note that, for many semiconductors, the broad optical structure appearing in the high-energy region consists of several contributions from different regions in the BZ. In particular, at room temperature or higher, thermal broadening makes it difficult to resolve individual contributions. Thus, the broad optical structure corresponding to the 8th oscillator may consist of multiple structures. The fit-determined parameters A, C, and E_0 for all eight T-L oscillators are listed in Table II.

Our ε spectrum is similar to the data reported in a previous SE study [33] of a polycrystalline $Cu_2ZnGeSe_4$ bulk in the spectral range of 1.2 to 4.6 eV. Three optical structures, assigned as the E_0, E_{1A}, and E_{1B} transitions, have been analyzed there and the transition energies were determined to be 1.41, 2.46, and 3.67 eV, respectively. Although their E_{1A} transition energy is close to our second oscillator energy (2.51 eV), the E_0 and E_{1B} transition energies are apparently different from our results of 1.25 eV (E_0) and 4.00 eV (Osc. #3). The observed small discrepancies in fit-determined transition energies between the two studies may be caused, in part, by the limited spectral range used in the previous SE study [33]. Their modeled spectrum deviates somewhat from the experimental data for both below 2.0 eV and above 3.5 eV, which possibly makes the extracted transition energies less accurate.

TABLE II. Best-fit parameters for the eight Tauc-Lorentz oscillators used to construct the ε spectrum of $Cu_2ZnGeSe_4$. The Tauc gap E_g in Eq. (2) is set to be the same, 1.19 ± 0.01 eV, for all the oscillators. The fit-determined $\varepsilon_1(\infty)$ is 1.18 ± 0.01.

Osc. No.	A [eV]	C [eV]	E_0 [eV]
1	20.73 ± 6.79	0.92 ± 0.05	1.25 ± 0.11
2	12.07 ± 0.32	1.01 ± 0.02	2.51 ± 0.00
3	8.18 ± 0.65	1.11 ± 0.03	4.00 ± 0.01
4	7.97 ± 1.52	1.39 ± 0.12	4.79 ± 0.03
5	3.15 ± 1.00	1.09 ± 0.10	5.36 ± 0.02
6	3.00 ± 0.36	1.18 ± 0.05	6.42 ± 0.01
7	1.70 ± 0.23	1.29 ± 0.06	7.27 ± 0.01
8	30.80 ± 1.77	6.20 ± 0.07	7.54 ± 0.13

In fact, determination of the E_0 has been an issue for kesterite solar cell materials [59]. In the case of $Cu_2ZnSnSe_4$, for example, a large discrepancy has been found among the reported E_0 (0.8 - 1.6 eV) depending on the sample preparation method and characterization technique. The E_0 of $Cu_2ZnSnSe_4$ is now believed to be ~1.0 eV based on several experimental studies and electronic structure calculations. In our previous temperature-dependent SE study [5] of $Cu_2ZnSnSe_4$, we employed the pseudo-bulk method and accurately determined the E_0 of 0.97 eV at room temperature.

In part due to a relatively small number of studies as well as the same problems encountered with $Cu_2ZnSnSe_4$, the E_0 of $Cu_2ZnGeSe_4$ has not yet been well established. The reported E_0 of $Cu_2ZnGeSe_4$ from previous studies and this work are compared in Table III. Some of the previous experimental studies estimated the E_0 by extrapolating the linear section of the absorption $(\alpha E)^2$ spectrum to zero. However, the linear section of the absorption curve can be defined somewhat ambiguously, which often leads to a large uncertainty in the estimated E_0. In our study, application of the pseudobulk method, which has been successfully used to determine the E_0 of $Cu_2ZnSnSe_4$ (Ref. 5) and Cu_2SnSe_3, [60] makes the

bandgap onset visible at ~1.2 eV even in the $<\varepsilon_2>$ spectrum as shown in Fig. 6(a). The E_0 was then obtained from the analytical modeling of the data, which improves the accuracy of result.

TABLE III. Bandgap energies in eV for $Cu_2ZnGeSe_4$ reported by this work and previous studies.

Bandgap energy (eV) - Experiment								
1.25[a]	1.41[b]	1.35[c]	1.35[d]	1.6[e]	1.4 – 1.43[f]	1.29[g]	1.5[h]	1.4[i]

Bandgap energy (eV) - Theory				
1.18 (KS)[a] 0.954 (ST)[a] 0.761 (PMCA)[a]	1.60 (KS)[j] 1.32 (ST)[j]	1.52[k]	1.5 (KS)[l] 1.32 (ST)[l] 1.21 (PMCA)[l]	1.1 (KS)[m] 0.76 (ST)[m]

[a] This work; [b] Ref. 33; [c] Ref. 61; [d] Ref. 62; [e] Ref. 53; [f] Ref. 63; [g] Ref. 52; [h] Ref. 64; [i] Ref. 65; [j] Ref. 66; [k] Ref. 7; [l] Ref. 41; [m] Ref. 67

The overall shape of the experimental ε spectrum (Fig. 6) shows good agreement with the calculated data shown in Figs. 3(a) through 3(c). However, the optical structure at ~2.5 eV appears much smaller than the main broad structure, and the main broad structure shows a "plateau"-looking top. Both features make the experimental ε spectrum look slightly different from the KS-phase ε data shown in Fig. 3(a). This suggests that the $Cu_2ZnGeSe_4$ crystal used in this study may not have a pure (ordered) KS phase. A similar discrepancy between the experimental spectrum and calculated KS-phase data has also been found for $Cu_2ZnSnSe_4$ [38]. However, differences in the calculated ε data among three structural phases are insignificant. Therefore, positive identification of the structural phase of $Cu_2ZnGeSe_4$ would require more systematic studies using other structural characterization techniques such as neutron scattering.

The optical structure at 2.51 eV is attributed mainly to the transition from the valence band characterized by the Cu 3*d* – Se 4*p* anti-bonding states to the Ge 5*s* – Se 4*p* anti-bonding states derived conduction bands. In fact, this transition is one of the noticeable characteristics of the optical function spectra for $Cu_2ZnSnSe_4$ and related compounds, and it has also been observed in the ε spectra for $Cu_2ZnSnSe_4$ [5,30,31,32,38], Cu_2ZnSnS_4 [28,29], and Cu_2SnSe_3 [31,60]. For the main broad structure, however, multiple transitions occur within a narrow spectral range, which makes it complicated to unambiguously assign individual electronic origin.

Complex refractive index $N = n + ik$, normal-incidence reflectivity R, and absorption coefficients α spectra can be calculated from the modeled ε data and are shown in Figs. 7(a) through 7(c). For comparison, the data for $Cu_2ZnSnSe_4$ are also included, which are obtained by modeling the room-temperature $<\varepsilon>$ spectrum shown in Ref. 5. In addition to lower E_0, $Cu_2ZnSnSe_4$ data also exhibit slightly sharper optical structures (dashed lines in Figs. 7(a) and 7(b)). Observation

of relatively weak and broad optical structures may suggest that $Cu_2ZnGeSe_4$ has a more disordered and/or defective structure than $Cu_2ZnSnSe_4$, which is not surprising considering the similar atomic sizes of Cu, Zn, and Ge.

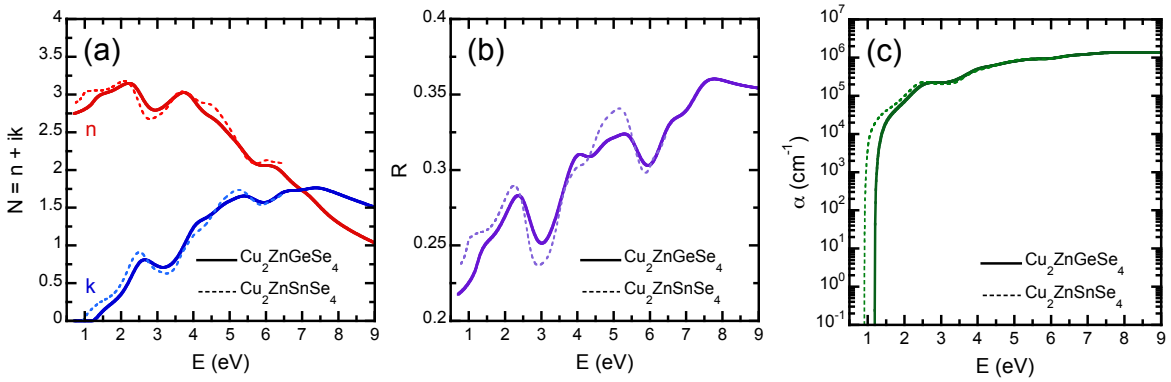

Figure 7. Fundamental optical function spectra for $Cu_2ZnGeSe_4$ calculated from the modeled ε data. (a) Complex refractive index N = n + ik, (b) normal-incidence reflectivity R, and (c) absorption coefficients α. For comparison, the spectra for $Cu_2ZnSnSe_4$ (dashed lines) are also included.

V. CONCLUSIONS

We studied the electronic structure and related fundamental optical properties of $Cu_2ZnGeSe_4$. The electronic energy band structure and complex dielectric function $\varepsilon = \varepsilon_1 + i\varepsilon_2$ spectra of $Cu_2ZnGeSe_4$ are obtained from *first-principles* calculations for kesterite (KS), stannite (ST), and primitive-mixed CuAu (PMCA) phases. Our calculations predict that the PMCA phase possesses an indirect bandgap ($E_0^{dir} - E_0^{ind} = 0.405$ eV) whereas the other two phases show a direct-bandgap transition. For the calculated ε spectra, all three phases show a similar shape composed of a weak but distinct structure at ~2.5 eV and a main broad structure spanning from 5 to 12 eV. However, the calculated electronic energy band structure shows that the KS phase has multiple interband transitions at ~2.5 eV between the Y and P points of the Brillouin zone, which may explain why the associated optical structure appears relatively strong in the ε_2 spectrum for the KS phase compared to the other phases. The calculated data were compared with the experimental ε spectrum determined by spectroscopic ellipsometry (SE). The experimental spectrum agrees well with the calculated ones but also implies the presence of disorder or mixed phases in the polycrystalline $Cu_2ZnGeSe_4$ film used in this work. By modeling the ellipsometric data with the sum of eight Tauc-Lorentz oscillators, we obtained the bandgap (E_0) and Tauc-gap (E_g) energies of 1.25 and 1.19 eV, respectively. Complex refractive index N = n + ik, normal-incidence reflectivity R, and absorption coefficients α were also calculated from the modeled ε spectrum, which were compared with the results of $Cu_2ZnSnSe_4$.

The overall N, R, and α spectra are similar between $Cu_2ZnGeSe_4$ and $Cu_2ZnSnSe_4$, as expected; however, the optical structures for $Cu_2ZnGeSe_4$ appear to be slightly weaker and broader than those for $Cu_2ZnSnSe_4$, in addition to the difference in the E_0. The weaker and broader characteristic of optical structures may suggest that $Cu_2ZnGeSe_4$ contains an increased number of structural imperfections such as Ge_{Zn}, $Ge_{Zn}+2Cu_{Zn}$, as well as $Cu_{Zn}+Zn_{Cu}$ defect complexes, which is, in part, due to the similar atomic sizes of Cu, Zn, and Ge. The results from our comparison study of experimental data analysis and first-principles calculations help to better understand the electronic structure of $Cu_2ZnGeSe_4$ and related physical properties. The fit-determined bandgap energy and fundamental optical function spectra reported in this work can also be used to design Ge-alloyed $Cu_2ZnSnSe_4$-based solar cells with the optimum bandgap and model their performance.

ACKNOWLEDGMENTS

This work was supported by the U.S. Department of Energy under Contract No. DE-AC36-08-GO28308 to the National Renewable Energy Laboratory.

REFERENCES

[1] See, for example, *Copper Zinc Tin Sulfide-Based Thin Film Solar Cells*, edited by K. Ito (John Wiley & Sons, Chichester, 2015).

[2] Y.S. Lee, T. Gershon, O. Gunawan, T.K. Todorov, T. Gokmen, Y. Virgus, and S. Guha, $Cu_2ZnSnSe_4$ thin-film solar cells by thermal co-evaporation with 11.6% efficiency and improved minority carrier diffusion length, Adv. Energy Mater. **5**, 1401372 (2015).

[3] M.A. Green, K. Emery, Y. Hishikawa, W. Warta, and E.D. Dunlop, Solar cell efficiency tables (Version 45), Prog. Photovolt: Res. Appl. **23**, 1 (2015).

[4] W. Shockley and H.J. Queisser, Detailed balance limit of efficiency of p-n junction solar cells, J. Appl. Phys. **32**, 510 (1961).

[5] S.G. Choi, T.J. Kim, S.Y. Hwang, J. Li, C. Persson, Y.D. Kim, S.-H. Wei, and I.L. Repins, Temperature dependent band-gap energy for $Cu_2ZnSnSe_4$: A spectroscopic ellipsometric study, Sol. Energy Mater. Sol. Cells **130**, 375 (2014).

[6] W. Wang, M.T. Winkler, O. Gunawan, T. Gokmen, T.K. Todorov, Y. Zhu, and D.B. Mitzi, Device characteristics of CZTSSe thin-film solar cells with 12.6% efficiency, Adv. Energy Mater. **4**, 1301465 (2014).

[7] Q. Shu, J.-H. Yang, S. Chen, B. Huang, H. Xiang, X.-G. Gong, and S.-H. Wei, $Cu_2Zn(Sn,Ge)Se_4$ and $Cu_2Zn(Sn,Si)Se_4$ alloys as photovoltaic materials: Structural and electronic properties, Phys. Rev. B **87**, 115208 (2013).

[8] S. Chen, A. Walsh, J.-H. Yang, X.G. Gong, L. Sun, P.-X. Yang, J.-H. Chu, and S.-H. Wei, Compositional dependence of structural and electronic properties of $Cu_2ZnSn(S,Se)_4$ alloys for thin film solar cells, Phys. Rev. B **83** ,125201 (2011).

[9] D.B. Mitzi, O. Gunawan, T.K. Todorov, K. Wang, and S. Guha, The path toward a high-performance solution-processed kesterite solar cell, Sol. Energy Mater. Sol. Cells, **95**, 1421 (2011).

[10] K. Wang, B. Shin, K.B. Reuter, T. Todorov, D.B. Mitzi, and S. Guha, Structural and elemental characterization of high efficiency Cu_2ZnSnS_4 solar cells, Appl. Phys. Lett. **98**, 051912 (2011).

[11] N. Vora, J. Blackburn, I. Repins, C. Beall, B. To, J. Pankow, G. Teeter, M. Young, and R. Noufi, Phase identification and control of thin films deposited by co-evaporation of elemental Cu, Zn, Sn, and Se, J. Vac. Sci. Technol. A **30**, 051201 (2012).

[12] A. Fairbrother, X. Fontané, V. Izquierdo-Roca, M. Placidi, D. Sylla, M. Espindola-Rodriguez, S. López-Mariño, F.A. Pulgarín, O. Vigil-Galán, A. Pérez-Rodriguez, and E. Saucedo, Secondary phase formation in Zn-rich $Cu_2ZnSnSe_4$-based solar cells annealed in low pressure and temperature conditions, Prog. Photovolt.: Res. Appl., **22**, 479 (2014).

[13] J. Just, D. Lützenkirchen-Hecht, R. Frahm, S. Schorr, and T. Unold, Determination of secondary phases in kesterite Cu_2ZnSnS_4 thin films by x-ray absorption near edge structure analysis, Appl. Phys. Lett. **99**, 262105 (2011).

[14] A. Reidinger, K. Hönes, X. Fontané, V. Izquierdo-Roca, E. Saucedo, N. Valle, A. Pérez-Rodríguez, and S. Siebentritt, Detection of a ZnSe secondary phase in coevaporated $Cu_2ZnSnSe_4$ thin films, Appl. Phys. Lett. **98**, 101907 (2011).

[15] T. Gokman, O. Gunawan, T.K. Todorov, and D.B. Mitzi, Band tailing and efficiency limitation in kesterite solar cells, Appl. Phys. Lett. **103**, 103506 (2013).

[16] C.J. Hages, S. Levcenco, C.K. Miskin, J.H. Alsmeier, D. Abou-Ras, R.G. Wilks, T. Unold, and R. Agrawal, Improved performance of Ge-alloyed CZTGeSSe thin-film solar cells through control of elemental losses, Prog. Photovolt.: Res. Appl. **23**, 376 (2015).

[17] S. Bag, O. Gunawan, T. Gokmen, Y. Zhu, and D.B. Mitzi, Hydrazine-processed Ge-substituted CZTSe solar cells, Chem. Mater. **24**, 4588 (2012).

[18] C. Persson, R. Chen, H. Zhao, M. Kumar, and D. Huang, in *Copper Zinc Tin Sulfide-Based Thin Film Solar Cells*, edited by K. Ito (John Wiley & Sons, Chichester, 2015), Ch. 4.

[19] A. Kanevce, I. Repins, and S.-H. Wei, Impact of bulk properties and local secondary phases on the $Cu_2(Zn,Sn)Se_4$ solar cells open-circuit voltage, Sol. Energy. Mater. Sol. Cells **133**, 119 (2015).

[20] R.E. Banai, L.A. Burton, S.G. Choi, F. Hofherr, T. Sorgenfrei, A. Walsh, B. To, A. Cröll, and J.R.S. Brownson, Ellipsometric characterization and density-functional theory analysis of anisotropic optical properties of single-crystal α-SnS, J. Appl. Phys. **116**, 013511 (2014).

[21] A. Thomasson, F. Ibrahim, C. Lefevre, E. Autissier, F. Roulland, C. Mény, C. Leuvrey, S. Choi, W. Jo, O. Crégut, G. Versini, S. Barre, M. Alouani, and N. Viart, Effects of iron concentration and cationic site disorder on the optical properties of magnetoelectric gallium ferrite thin films, RSC Adv. **3**, 3124 (2013).

[22] D.E. Aspnes, Spectroscopic ellipsometry – A perspective, J. Vac. Sci. Technol. A **31**, 058502 (2013).

[23] H. Arwin and D.E. Aspnes, Nondestructive analysis of $Hg_{1-x}Cd_xTe$ (x = 0.00, 0.20, 0.29, and 1.00) by spectroscopic ellipsometry. II. Substrate, oxide, and interface properties, J. Vac. Sci. Technol. A **2**, 1316 (1984).

[24] J. Li, J. Chen, and R.W. Collins, Broadening of optical transitions in polycrystalline CdS and CdTe thin films, Appl. Phys. Lett. **97**, 181909 (2010).

[25] M.I. Alonso, M. Garriga, C.A. Durante Rincón, E. Hernández, and M. León, Optical functions of chalcopyrite $CuGa_xIn_{1-x}Se_2$ alloys, Appl. Phys. A **74**, 659 (2002).

[26] S.-H. Han, C. Persson, F.S. Hasoon, H.A. Al-Thani, A.M. Hermann, and D.H. Levi, Optical properties and electronic structures of $(4CuInSe_2)_y(CuIn_5Se_8)_{1-y}$, Phys. Rev. B **74**, 085212 (2006).

[27] S. Minoura, K. Kodera, T. Maekawa, K. Miyazaki, S. Niki, and H. Fujiwara, Dielectric function of $Cu(In,Ga)Se_2$-based polycrystalline materials, J. Appl. Phys. **113**, 063505 (2013).

[28] S. Levcenko, G. Gurieva, M. Guc, and A. Nateprov, Optical constants of Cu_2ZnSnS_4 bulk crystals, Moldavian J. Phys. Sci. **8**, 173 (2009).

[29] J. Li, H. Du, J. Yarbrough, A. Norman, K. Jones, G. Teeter, F.L. Terry Jr., and D. Levi, Spectral optical properties of Cu_2ZnSnS_4 thin film between 0.73 and 6.5 eV, Opt. Express **20**, A327 (2012).

[30] S. Ozaki and T. Namba, Optical properties and electronic band structure of $Cu_2ZnSnSe_4$ kesterite semiconductor, Phys. Status Solidi C **9**, 2403 (2012).

[31] Y. Hirate, H. Tampo, S. Minoura, H. Kadowaki, A. Nakane, K.M. Kim, H. Shibata, S. Niki, and H. Fujiwara, Dielectric functions of $Cu_2ZnSnSe_4$ and Cu_2SnSe_3 semiconductors, J. Appl. Phys. **117**, 015702 (2015).

[32] M. León, S. Levcenko, R. Serna, I.V. Bodnar, A. Nateprov, M. Guc, G. Gurieva, N. Lopez, J.M. Merino, R. Caballero, S. Schorr, A. Perez-Rodriguez, and E. Arushanov, Spectroscopic ellipsometry study of $Cu_2ZnSnSe_4$ bulk crystals, Appl. Phys. Lett. **105**, 061909 (2014).

[33] M. León, S. Levcenko, R. Serna, A. Nateprov, G. Gurieva, J.M. Merino, S. Schorr, and E. Arushanov, Spectroscopic ellipsometry study of $Cu_2ZnGeSe_4$ and $Cu_2ZnSiSe_4$ poly-crystals, Mater. Chem. Phys. **141**, 58 (2013).

[34] S. Adachi, Model dielectric constants of GaP, GaAs, GaSb, InP, InAs, and InSb, Phys. Rev. B **35**, 7454 (1987).

[35] S. Chen, X.G. Gong, A. Walsh, and S.-H. Wei, Crystal and electronic band structure of Cu_2ZnSnX_4 (X = S and Se) photovoltaic absorbers: Frist-principles insights, Appl. Phys. Lett. **94**, 041903 (2009).

[36] C. Persson, Electronic and optical properties of Cu_2ZnSnS_4 and $Cu_2ZnSnSe_4$, J. Appl. Phys. **107**, 053710 (2010).

[37] G. Rey, A. Redinger, J. Sendler, T.P. Weiss, M. Thevenin, M. Guennou, B. El Adib, and S. Siebentritt, The band gap of $Cu_2ZnSnSe_4$: Effect of order-disorder, Appl. Phys. Lett. **105**, 112106 (2014).

[38] S.G. Choi, H.Y. Zhao, C. Persson, C.L. Perkins, A.L. Donohue, B. To, A.G. Norman, J. Li, and I.L. Repins, Dielectric function spectra and critical-point energies of $Cu_2ZnSnSe_4$ from 0.5 to 9.0 eV, J. Appl. Phys. **111**, 033506 (2012).

[39] S. Schorr, The crystal structure of kesterite type compounds: A neutron and X-ray diffraction study, Sol. Energy Mater. Sol. Cells **95**, 1482 (2011).

[40] T. Washio, H. Nozaki, T. Fukano, T. Motohiro, K. Jimbo, and H. Katagiri, Analysis of lattice site occupancy in kesterite structure of Cu_2ZnSnS_4 films using synchrotron radiation x-ray diffraction, J. Appl. Phys. **110**, 074511 (2011).

[41] S. Chen, X. G. Gong, A. Walsh, and S.-H. Wei, Electronic structure and stability of quaternary chalcogenide semiconductors derived from cation cross-substitution of II-VI and I-III-VI_2 compounds, Phys. Rev. B **79**, 165211 (2009).

[42] J. Heyd, G. E. Scuseria, and M. Ernzerhof, Hybrid functionals based on a screened Coulomb potential, J. Chem. Phys. **118**, 8207 (2003).

[43] G. Kresse and J. Furthmüller, Efficient iterative schemes for ab initio total-energy calculations using a plane-wave basis set, Phys. Rev. B **54**, 11169 (1996).

[44] J.-S. Park, J.-H. Yang, A. Kanevce, S. Choi, I.L. Repins, and S.-H. Wei, Ordering-induced direct-to-indirect band gap transition in multication semiconductor compounds, Phys. Rev. B **91**, 075204 (2015).

[45] O.V. Parasyuk, L.D. Gulay, Y.E. Romanyuk, and L.V. Priskach, Phase diagram of the Cu_2GeSe_3-ZnSe system and crystal structure of the $Cu_2ZnGeSe_4$ compound, J. Alloys and Compounds **329**, 202 (2001).

[46] J.C. Phillips and G. Lucovsky, *Bonds and Bands in Semiconductors*, 2nd Ed. (Momentum Press, New York, 2009).

[47] I. Repins, C. Beall, N. Vora, C. DeHart, D. Kuciauskas, P. Dippo, B. To, J. Mann, W.C. Hsu, A. Goodrich, and R. Noufi, Co-evaporated $Cu_2ZnSnSe_4$ films and devices, Sol. Energy Mater. Sol. Cells **101**, 154 (2012).

[48] J. Scragg, P.J. Dale, D. Colombara, and L.M. Peter, Thermodynamic aspects of the synthesis of thin-film materials for solar cells, ChemPhysChem **13**, 3035 (2012).

[49] J.J. Scragg, T. Ericson, T. Kubart, M. Edoff, and C. Platzer-Björkman, Chemical insights into the instability of Cu_2ZnSnS_4 films during annealing, Chem. Mater. **23**, 4625 (2011).

[50] S. Chen, L.-W. Wang, A. Walsh, X.G. Gong, and S.-H. Wei, Abundance of $Cu_{Zn}+Sn_{Zn}$ and $2Cu_{Zn}+Sn_{Zn}$ defect clusters in kesterite solar cells, Appl. Phys. Lett. **101**, 223901 (2012).

[51] See Supplemental Material at URL (*to be inserted by publisher*) for cross-sectional scanning electron micrograph and a brief information on resulting device.

[52] D.M. Schleich and A. Wold, Optical and electrical properties of quaternary chalcogenides, Mater. Res. Bull. **12**, 111 (1977).

[53] H. Matsushita, T. Maeda, A. Katsui, and T. Takizawa, Thermal analysis and synthesis from the melts of Cu-based quaternary compounds Cu-III-IV-VI_4 and Cu_2-II-IV-VI_4 (II = Zn, Cd; III = Ga, In; IV = Ge, Sn; VI = Se), J. Cryst. Growth **208**, 416 (2000).

[54] M. Guc, S. Levcenko, V. Izquierdo-Roca, X. Fontané, E. Arushanov, and A. Pérez-Rodríguez, Polarized Raman scattering analysis of $Cu_2ZnSnSe_4$ and $Cu_2ZnGeSe_4$ single crystals, J. Appl. Phys. **114**, 193514 (2013).

[55] M. Grossberg, K. Timmo, T. Raadik, E. Kärber, V. Mikli, and J. Krustok, Study of structural and optoelectronic properties of $Cu_2Zn(Sn_{1-x}Ge_x)Se_4$ (x = 0 to 1) alloy compounds, Thin Solid Films **582**, 176 (2014).

[56] G.E. Jellison, Jr., L.A. Boatner, D.H. Lowdnes, R.A. McKee, and M. Godbole, Optical functions of transparent thin films of $SrTiO_3$, $BaTiO_3$, and SiO_x determined by spectroscopic ellipsometry, Appl. Opt. **33**, 6053 (1994).

[57] C.M. Nelson, M. Spies, L.S. Abdallah, S. Zollner, Y. Xu, and H. Luo, Dielectric function of $LaAlO_3$ from 0.8 to 6 eV between 77 and 700K, J. Vac. Sci. Technol. A **30**, 061404 (2012).

[58] G.E. Jellison, Jr. and F.A. Modine, Parameterization of the optical functions of amorphous materials in the interband region, Appl. Phys. Lett. **69**, 371 (1996); "Erratum," *ibid*. **69**, 2137 (1996).

[59] S. Ahn, S. Jung, J. Gwak, A. Cho, K. Shin, K. Yoon, D. Park, H. Cheong, and J.H. Yun, Determination of band gap energy (E_g) of $Cu_2ZnSnSe_4$ thin films: On the discrepancies of reported band gap values, Appl. Phys. Lett. **97**, 021905 (2010).

[60] S.G. Choi, J. Kang, J. Li, H. Haneef, N.J. Podraza, C. Beall, S.-H. Wei, S.T. Christensen, and I.L. Repins, Optical function spectra and bandgap energy of Cu_2SnSe_3, Appl. Phys. Lett. **106**, 043902 (2015).

[61] M. Morihama, F. Gao, T. Maeda, and T. Wada, Crystallographic and optical properties of $Cu_2Zn(Sn_{1-x}Ge_x)Se_4$ solid solution, Jpn. J. Appl. Phys. **53**, 04ER09 (2014).

[62] K. Timmo M. Kauk-Kuusik, M. Altosaar, J. Raudoja, M. Grossberg, T. Varema, M. Pilvet, I. Leinemann, O. Volobujiva, and E. Mellikov, Novel Cu_2CdSnS_4 and $Cu_2ZnGeSe_4$ absorber materials for monograin layer solar cell application, 28th European Photovolt. Solar Energy Conf. Exhibit. (2014) p. 2385.

[63] D.B. Khadka and J. Kim, Study of structural and optical properties of kesterite Cu_2ZnGeX_4 (X = S, Se) thin films synthesized by chemical spray pyrolysis, Cryst. Eng. Comm. **15**, 10500 (2013).

[64] M. Buffière, H. ElAnzeery, S. Queslati, K. Ben Messaoud, G. Brammertz, M. Meuris, and J. Poortmans, Physical characterization of $Cu_2ZnGeSe_4$ thin films from annealing of Cu-Zn-Ge precursor layers, Thin Solid Films **582**, 171 (2015).

[65] C.P. Heinrich, T.W. Day, W.G. Zeier, G.J. Snyder, and W. Tremel, Effect of isovalent substitution on the thermoelectric properties of the $Cu_2ZnGeSe_{4-x}S_x$ series of solid solutions, J. Am. Chem. Soc. **136**, 442 (2014).

[66] D. Chen and N.M. Ravindra, Electronic and optical properties of Cu_2ZnGeX_4 (X = X, Se, and Te) quaternary semiconductors, J. Alloys Compd. **579**, 468 (2013).

[67] S. Nakamura, T. Maeda, and T. Wada, Phase stability and electronic structure of In-free photovoltaic materials: $Cu_2ZnSiSe_4$, $Cu_2ZnGeSe_4$, and $Cu_2ZnSnSe_4$, Jpn. J. Appl. Phys. **49**, 121203 (2010).